ELSEVIER

Comput. Methods Appl. Mech. Engrg. 191 (2001) 611–634

Computer methods in applied mechanics and engineering

www.elsevier.com/locate/cma

Computation of flows in supersonic wind-tunnels

Sanjay Mittal *, Satish Yadav

Department of Aerospace Engineering, Indian Institute of Technology, Kanpur, UP 208 016, India

Received 3 January 2000; received in revised form 13 November 2000

Abstract

Results are presented for finite-element computation of flows in supersonic wind-tunnels. It is demonstrated that the stabilized finite-element methods can be utilized to design and analyze supersonic wind-tunnels in general and the diffuser section in particular. The computations are capable of simulating the *start-up* problems associated with the wind-tunnels that are equipped with narrow diffusers and do not allow the start-up shock to pass through. The effect of various component geometries is investigated. It is shown, via examples, that the method may be used to find close to optimal values of the geometric parameters of the supersonic diffuser. A nozzle block that is designed purely by the method of characteristics, without boundary-layer corrections, fails to deliver a uniform flow in the test-section. In certain cases, even though a certain stagnation to exit pressure ratio may be able to *start* the tunnel, a higher pressure ratio may be desirable for better flow quality. Results for two benchmark problems, one involving flow in a double throat nozzle and the other a Mach 3 flow over a compression corner, have also been presented to establish confidence in the computations.

Keywords: Unsteady flow; Supersonic; Wind-tunnels; Diffusers; Start-up problem

1. Introduction

This paper demonstrates the capability of the stabilized finite-element methods in the design and analysis of supersonic wind-tunnels. A supersonic wind-tunnel consists of a nozzle block, test-section and a diffuser. Details on the various aspects of the supersonic wind-tunnel and its components can be found in the text by Anderson [1,2]. High-speed internal flows are complex and are often associated with shock-wave/boundary-layer interactions. Internal flows have been investigated by several researchers in the past. A review of the data-base available for shock-wave/boundary-layer interactions in supersonic inlets has been presented by Hamed and Shang [3]. Polsky and Cambier [4] studied the transient flow through a shock tunnel using Euler equations. Chen and Chakravarthy [5] used the Reynolds-averaged Navier–Stokes equations to study separated flow through converging–diverging nozzles and Argrow and Emanuel [6] investigated the transonic flow field in a two-dimensional minimum length nozzle. Causon et al. [7] have applied their high resolution shock-capturing methods, using Euler equations, to study surge in aircraft engine intakes. Reddy and Weir [8] have simulated three-dimensional flow in a Mach = 5 inlet and compared it with experimental results. Some of the studies have also incorporated the effect of *bleed* and bypass systems in supersonic inlet flows [9,10]. Work has also been done by several researchers on air intakes for scramjet applications using, both, Euler [11] and Navier–Stokes equations [12–14]. It appears that there have been a number of successful studies with the Euler equations, however, there have been relatively fewer efforts to address the complex details of the shock-wave/boundary-layer interactions in internal flows.

* Corresponding author. Tel.: +512-597-253, +512-597-626; fax: +512-590-260.
E-mail address: smittal@iitk.ac.in (S. Mittal).

0045-7825/01/$ - see front matter
PII: S0045-7825(01)00305-X

The governing equations for the flow are the compressible Navier–Stokes equations in the conservation law form. They are solved using a stabilized finite-element formulation based on conservation variables. The streamline-upwind/Petrov–Galerkin (SUPG) stabilization technique is employed to stabilize the computations against spurious numerical oscillations due to advection-dominated flows [15–19]. A shock-capturing term is added to the formulation to provide stability to the computations in the presence of discontinuities and large gradients in the flow. Some of the computations reported in this paper are carried out using the enhanced-discretization interface-capturing technique (EDICT) that was introduced by Tezduyar et al. [20,21] for simulation of unsteady flow problems with interfaces such as two-fluid and free-surface flows. Later Mittal et al. [22] demonstrated, through certain examples, the application of EDICT to unsteady compressible flow problems. This technique is useful in accurate computation of unsteady flows that involve shock-wave/boundary-layer interactions. A base mesh called the *Level-0* mesh is utilized to initiate the computations. An error indicator, proposed by Lohner [23], is employed to identify the regions in the computational domain that need enhanced discretization for increased accuracy. The elements that are chosen for enhanced discretization are either subdivided into four or 16 elements. The resulting finite-element mesh is referred to as either a *Level-1* mesh or a *Level-2* mesh. Usually, the regions of element refinement are the ones that are associated with large gradients of the flow variables. The finite-element functions corresponding to enhanced discretization are designed to have two components, with each component coming from a different level of mesh refinement over the same computational domain.

The application of the base finite-element formulation to various flow problems involving external flow past cylinders and airfoils in various speed regimes has been reported in earlier papers [18,19]. In this paper the method is applied to the computation of flows in supersonic wind-tunnels. One of the interesting components in the wind-tunnel is the diffuser section that is located just downstream of the test-section. It is responsible for slowing the flow and recovery of static pressure via a train of oblique shocks and viscous action. The flow in the diffuser is extremely complex and involves shock-wave/boundary-layer interactions. Before the method is applied to the computation of flows in wind-tunnels it is validated via a couple of benchmark problems. The first one is the Mach 3 flow past a 10° compression corner. This problem involves supersonic flow past a flat plate followed by a compression corner that results in an interesting shock-wave/boundary-layer interaction. The results compare quite well with those reported by Shakib [24], Carter [25] and Hung and MacCormack [26]. The second benchmark problem is the flow in a double throat nozzle. Results for this problem have been computed by other researchers and reported in a *GAMM workshop* [27]. The results with the present formulation are in excellent comparison with those reported by others. The phenomenon of *unstarting* of the tunnel due to insufficient area of the diffuser throat to allow the *start-up* shock to pass through has been simulated. The effect of various parameters of the tunnel including the stagnation to exit pressure ratio have been studied. Nozzle blocks designed with and without boundary-layer corrections have been used to study the tunnel performance. A useful tool has been developed that may be utilized for the design of diffuser sections of wind-tunnels or aircraft engine intakes.

The equation systems resulting from the finite-element discretization of the flow problems are solved iteratively using a matrix-free technique to reduce the memory requirements. This vector-based technique [28] eliminates the need to compute or store any coefficient matrices including those at the element level. The method has been implemented on a shared-memory parallel multi-processor computer from *SGI*.

In Section 2 the governing equations for compressible fluid flow are reviewed. The stabilized formulations along with the description for enhanced discretization are described in Section 3. Results and discussion constitute Section 4 and a few concluding remarks are made in Section 5.

2. The governing equations

Let $\Omega \subset \mathbb{R}^{n_{sd}}$ and $(0, T)$ be the spatial and temporal domains respectively, where n_{sd} is the number of space dimensions, and let Γ denote the boundary of Ω. The spatial and temporal coordinates are denoted by $\mathbf{x}$ and t. The Navier–Stokes equations governing the fluid flow, in conservation form, are

$$\frac{\partial \rho}{\partial t} + \nabla \cdot (\rho \mathbf{u}) = 0 \quad \text{on } \Omega \text{ for } (0,T), \tag{1}$$

$$\frac{\partial (\rho \mathbf{u})}{\partial t} + \nabla \cdot (\rho \mathbf{u}\mathbf{u}) + \nabla p - \nabla \cdot \mathbf{T} = \mathbf{0} \quad \text{on } \Omega \text{ for } (0,T), \tag{2}$$

$$\frac{\partial (\rho e)}{\partial t} + \nabla \cdot (\rho e \mathbf{u}) + \nabla \cdot (p\mathbf{u}) - \nabla \cdot (\mathbf{T}\mathbf{u}) + \nabla \cdot \mathbf{q} = 0 \quad \text{on } \Omega \text{ for } (0,T), \tag{3}$$

where ρ, $\mathbf{u}$, p, $\mathbf{T}$, e and $\mathbf{q}$ are the density, velocity, pressure, viscous stress tensor, the total energy per unit mass and the heat flux vector, respectively. The viscous stress tensor is defined as

$$\mathbf{T} = \mu\Big((\nabla \mathbf{u}) + (\nabla \mathbf{u})^{\mathrm{T}}\Big) + \lambda(\nabla \cdot \mathbf{u})\mathbf{I}, \tag{4}$$

where μ and λ are the viscosity coefficients. It is assumed that μ and λ are related by

$$\lambda = -\frac{2}{3}\mu. \tag{5}$$

Pressure is related to the other variables via the equation of state. For ideal gases, the equation of state assumes the special form

$$p = (\gamma - 1)\rho i, \tag{6}$$

where γ is the ratio of specific heats and i is the internal energy per unit mass that is related to the total energy per unit mass and velocity as

$$i = e - \frac{1}{2}\|\mathbf{u}\|^2. \tag{7}$$

The heat flux vector is defined as

$$\mathbf{q} = -\kappa \nabla \theta, \tag{8}$$

where κ is the heat conductivity and θ is the temperature. The temperature is related to the internal energy by the following relation:

$$\theta = \frac{\gamma - 1}{R} i, \tag{9}$$

where R is the ideal gas constant. Prandtl number (P_r), assumed to be specified, relates the heat conductivity to the fluid viscosity according to the following relation:

$$\kappa = \frac{\gamma R \mu}{(\gamma - 1)P_r}. \tag{10}$$

The compressible Navier–Stokes equations (1)–(3) can be written in the conservation variables

$$\frac{\partial \mathbf{U}}{\partial t} + \frac{\partial \mathbf{F}_i}{\partial x_i} - \frac{\partial \mathbf{E}_i}{\partial x_i} = \mathbf{0} \quad \text{on } \Omega \text{ for } (0,T),$$

where $\mathbf{U} = (\rho, \rho u_1, \rho u_2, \rho e)$ is the vector of conservation variables and $\mathbf{F}_i$ and $\mathbf{E}_i$ are, respectively, the Euler and viscous flux vectors defined as

$$\mathbf{F}_i = \begin{matrix} u_i \rho \\ u_i \rho u_1 + \delta_{i1} p \\ u_i \rho u_2 + \delta_{i2} p \\ u_i(\rho e + p) \end{matrix}$$

$$\mathbf{E}_i = \begin{pmatrix} 0 \\ \tau_{i1} \\ \tau_{i2} \\ -q_i + \tau_{ik}u_k \end{pmatrix}, \tag{13}$$

where u_i, q_i and τ_{ik} are the components of the velocity, heat flux and viscous stress tensor, respectively. In the quasi-linear form, Eq. (11) is written as

$$\frac{\partial \mathbf{U}}{\partial t} + \mathbf{A}_i \frac{\partial \mathbf{U}}{\partial x_i} - \frac{\partial}{\partial x_i}\left(\mathbf{K}_{ij}\frac{\partial \mathbf{U}}{\partial x_j}\right) = \mathbf{0} \quad \text{on } \Omega \text{ for } (0,T), \tag{14}$$

where

$$\mathbf{A}_i = \frac{\partial \mathbf{F}_i}{\partial \mathbf{U}} \tag{15}$$

is the Euler Jacobian matrix and $\mathbf{K}_{ij}$ is the diffusivity matrix satisfying

$$\mathbf{K}_{ij}\frac{\partial \mathbf{U}}{\partial x_j} = \mathbf{E}_i. \tag{16}$$

Corresponding to Eq. (14), the following boundary and initial conditions are chosen

$$\mathbf{U} = \mathbf{g} \quad \text{on } \Gamma_g \text{ for } (0,T), \tag{17}$$

$$\mathbf{n}\cdot\mathbf{E} = \mathbf{h} \quad \text{on } \Gamma_h \text{ for } (0,T), \tag{18}$$

$$\mathbf{U}(\mathbf{x},0) = \mathbf{U}_0 \quad \text{on } \Omega. \tag{19}$$

3. Finite-element formulation

Consider a finite-element discretization of Ω into subdomains Ω^e, $e = 1,2,\ldots,n_{\text{el}}$, where n_{el} is the number of elements. Based on this discretization, we define the finite-element trial function space $\mathscr{S}^h$ and weighting function space $\mathscr{V}^h$. These function spaces are selected, by taking the Dirichlet boundary conditions into account, as subsets of $[\mathbf{H}^{1h}(\Omega)]^{n_{\text{dof}}}$, where $\mathbf{H}^{1h}(\Omega)$ is the finite-dimensional function space over Ω and n_{dof} is the number of degrees of freedom:

$$\mathscr{S}^h = \left\{\mathbf{U}^h \,|\, \mathbf{U}^h \in \left[\mathbf{H}^{1h}(\Omega)\right]^{n_{\text{dof}}},\ \mathbf{U}^h|_{\Omega^e} \in \left[P^1(\Omega^e)\right]^{n_{\text{dof}}},\ \mathbf{U}^h\cdot\mathbf{e}_k \doteq g_k \text{ on } \Gamma_{g_k}\right\},$$
$$\mathscr{V}^h = \left\{\mathbf{W}^h \,|\, \mathbf{W}^h \in \left[\mathbf{H}^{1h}(\Omega)\right]^{n_{\text{dof}}},\ \mathbf{W}^h|_{\Omega^e} \in \left[P^1(\Omega^e)\right]^{n_{\text{dof}}},\ \mathbf{W}^h\cdot\mathbf{e}_k \doteq 0 \text{ on } \Gamma_{g_k}\right\} \tag{21}$$

where $[P^1(\Omega^e)]$ represents the first-order polynomial in Ω^e and $k = 1,\ldots,n_{\text{dof}}$. The stabilized finite-element formulation of Eq. (14) is written as follows: find $\mathbf{U}^h \in \mathscr{S}^h$ such that $\forall \mathbf{W}^h \in \mathscr{V}^h$,

$$\int_\Omega \mathbf{W}^h\cdot\left(\frac{\partial \mathbf{U}^h}{\partial t} + \mathbf{A}_i^h\frac{\partial \mathbf{U}^h}{\partial x_i}\right)\mathrm{d}\Omega + \int_\Omega \left(\frac{\partial \mathbf{W}^h}{\partial x_i}\right)\cdot\left(\mathbf{K}_{ij}^h\frac{\partial \mathbf{U}^h}{\partial x_j}\right)\mathrm{d}\Omega + \sum_{e=1}^{n_{\text{el}}}\int_{\Omega^e}\tau\left(\mathbf{A}_k^h\right)^{\mathrm{T}}\left(\frac{\partial \mathbf{W}^h}{\partial x_k}\right)$$
$$\left[\frac{\partial \mathbf{U}^h}{\partial t} + \mathbf{A}_i^h\frac{\partial \mathbf{U}^h}{\partial x_i} - \frac{\partial}{\partial x_i}\left(\mathbf{K}_{ij}^h\frac{\partial \mathbf{U}^h}{\partial x_j}\right)\right]\mathrm{d}\Omega + \sum_{e=1}^{n_{\text{el}}}\int_{\Omega^e}\delta\left(\frac{\partial \mathbf{W}^h}{\partial x_i}\right)\cdot\left(\frac{\partial \mathbf{U}^h}{\partial x_i}\right)\mathrm{d}\Omega = \int_{\Gamma_h}\mathbf{W}^h\cdot\mathbf{h}^h\,\mathrm{d}\Gamma. \tag{22}$$

In the variational formulation given by Eq. (22), the first two terms and the right-hand side constitute the Galerkin formulation of the problem. The first series of element-level integrals in Eq. (22) are the SUPG stabilization terms added to the variational formulation to stabilize the computations against node-to-node oscillations in the advection-dominated range. The second series of element-level integrals in the formulation are the shock-capturing terms that stabilize the computations in the presence of sharp gradients. The

stabilization coefficients δ and τ are the ones that are used by Mittal [18] and Mittal et al. [29] and quite similar to those employed by Aliabadi and Tezduyar [30]. They are defined as

$$= \max[0, \tau_a - \tau_\delta],$$

$$\left(\left(\frac{2(c + \|\mathbf{u}\|)}{h} \right) + \left(\frac{12\nu}{h^2} \right)^2 \right)^{-} \mathbf{I},$$

$$\tau_\delta = \frac{\delta}{2(c + \|\mathbf{u}\|)^2} \mathbf{I},$$

$$\delta = \left[\frac{\left\| \frac{\partial \mathbf{U}}{\partial t} + \mathbf{A}_i \frac{\partial \mathbf{U}}{\partial x_i} \right\|_{\mathbf{A}_0^{-1}}}{\left\| J_{1i} \frac{\partial \mathbf{U}}{\partial x_i} \right\|_{\mathbf{A}_0^{-1}} + \left\| J_{2i} \frac{\partial \mathbf{U}}{\partial x_i} \right\|_{\mathbf{A}_0^{-1}}} \right]$$

where c is the wave speed, h is the element length, J_{jk} are the components of Jacobian transformation matrix from physical to the local coordinates and $\mathbf{A}_0^{-1}$ is the inverse of Reimannian metric tensor related to the transformation between the conservation and entropy variables [31]. Matrix τ_δ is subtracted from τ_a to account for the shock-capturing term as shown in Eq. (23).

The time discretization of the variational formulation given by Eq. (22) is done via the generalized trapezoidal rule. For unsteady computations, we employ a second-order accurate-in-time procedure.

4. Results and discussions

All the computations reported in this paper are carried out in 64 bit precision using linear triangular elements on the shared-memory parallel computers of the SGI multiple-processor systems (*Origin-200*). The non-linear equation systems resulting from the finite-element discretization of the flow equations are solved using the Generalized Minimal RESidual (GMRES) technique [32] in conjunction with block-diagonal preconditioners. Sarkis et al. [33] have reported results for a new variant of the Schwarz preconditioned (GMRES) methods for unsteady compressible flow calculations with various preconditioners and for various values of the Courant number. The interested reader is referred to their paper for an interesting discussion on the performance of various preconditioners in the context of unsteady compressible flows. For all the cases, unless mentioned otherwise, the viscosity and thermal conductivity coefficients are constant. The Prandtl number is 0.72 and the ratio of specific heats, γ, is 1.4. All the results are for laminar flows and no turbulence model has been used.

4.1. $M = 3$, $Re = 16{,}800$ flow past a compression corner

In this problem Mach 3 flow passes over a flat plate and then a compression corner of 10°. This is one of the test cases studied by Carter [25] and the flow conditions are identical to the ones described by him. The computational domain covers the area $-0.2 \leqslant x \leqslant 1.8$, $0 \leqslant y \leqslant 0.575$ on the plate and a height of 0.575 above the wall past the corner. The flat plate is placed at $x = 0$ and the 10° corner at $x = 1.0$. At the inflow and top boundary all flow variables are specified. On the solid surface (plate and the compression ramp) no-slip condition is specified on the velocity while the wall temperature is prescribed as the stagnation temperature of the free-stream flow. Symmetry conditions are specified on the line of symmetry for $x < 0$, $y = 0$ while no conditions are specified on the outflow boundary. The Reynolds number based on the distance between the leading edge of the plate and compression corner is 16,800. The dependence of the viscosity on the temperature is modeled via Sutherland's law of viscosity. A mesh with 5386 nodes and 10,520 triangular elements is utilized to compute the solution. Once the steady-state solution is realized it is used to compute the solution on the *Level-2* mesh. Fig. 1 shows the mesh for the *Level-2* computations and the steady-state Mach number, pressure, density and temperature fields. The leading-edge shock due to the development of boundary-layer on the flat plate has been captured quite well. The separation of the flow ahead of the corner and its subsequent reattachment downstream of the corner results in a region of recirculation which

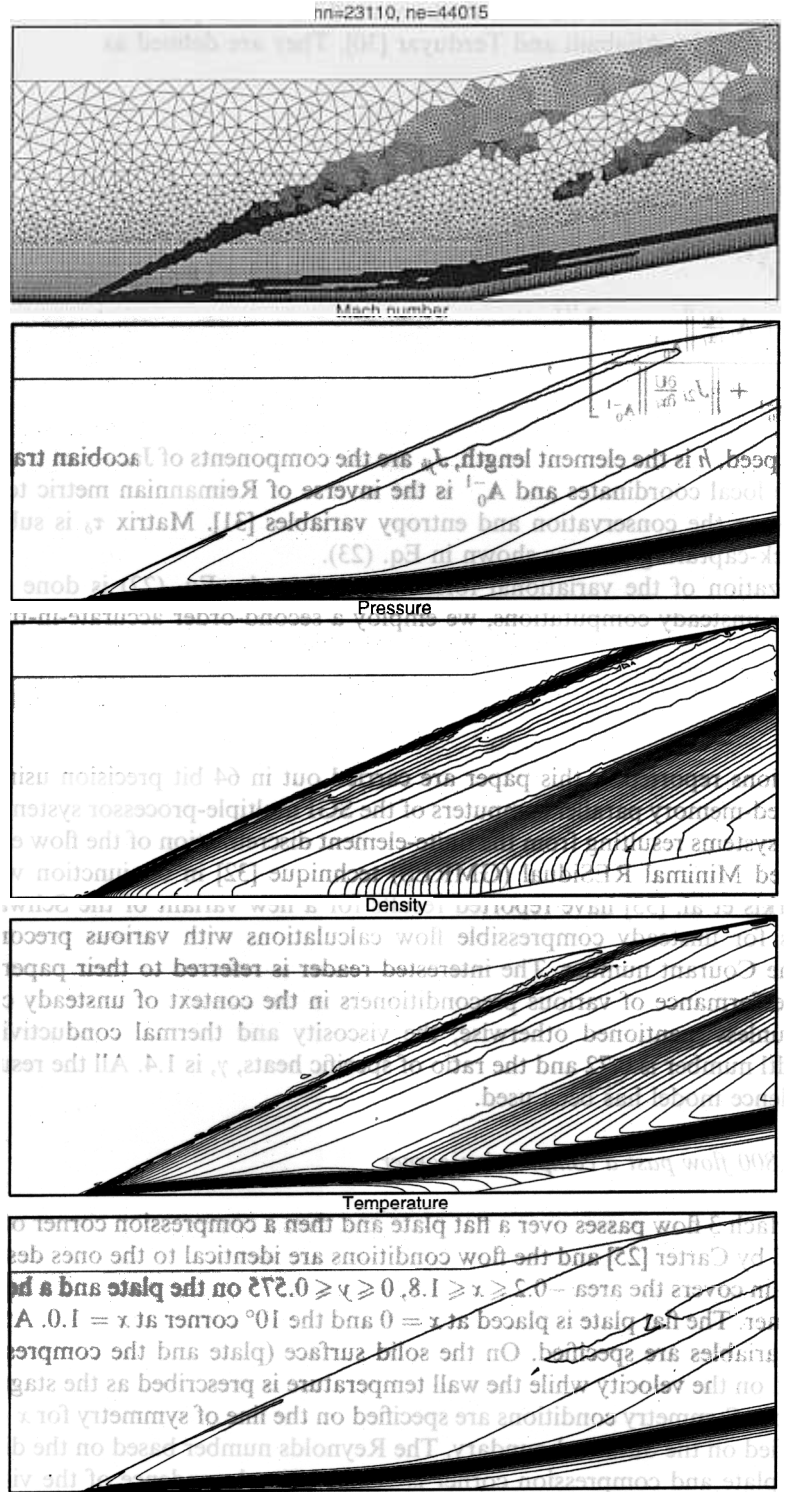

Fig. 1. $Re = 16{,}800$, $M = 3$ flow over a compression corner: the *Level-2* mesh and the computed flow field for the steady-state solution.

can be observed in the solution. The error indicator picks up the regions in the flows that involve shocks and shear layer and the corresponding elements are refined to improve the accuracy of the computation. The solution obtained with the base mesh (*Level-0*) shows a similar behavior except that the solution with

Level-2 mesh has crisper shocks. The separation point of the flow for the present calculations is at $x = 0.89$. Shakib [24], Hung and MacCormack [26] and Carter [25] have reported this value to be 0.88, 0.89 and 0.84, respectively, for their computations. It is interesting to contrast this solution to that for the inviscid flow case. In the absence of viscosity, there is no boundary-layer and an oblique shock is expected at the compression corner. In the present case, due to viscous effects, the oblique shock is replaced by a compression fan. Fig. 2 shows the variation of the pressure and the skin friction coefficients on the solid surface. It can be observed that the curves obtained with the *Level-0* and *Level-2* meshes are almost identical. The results compare quite well with those obtained with other researchers. This test problem validates the ability of the present method in the computation of flows that involve shock-wave/boundary-layer interactions which are a significant feature in the flows in supersonic wind-tunnels and diffusers.

4.2. Flow in a double throat nozzle

This problem was one of the test cases for a GAMM-workshop [27] and was designed with the aim of generating strong viscous interaction phenomenon in steady, laminar, compressible internal flows. The

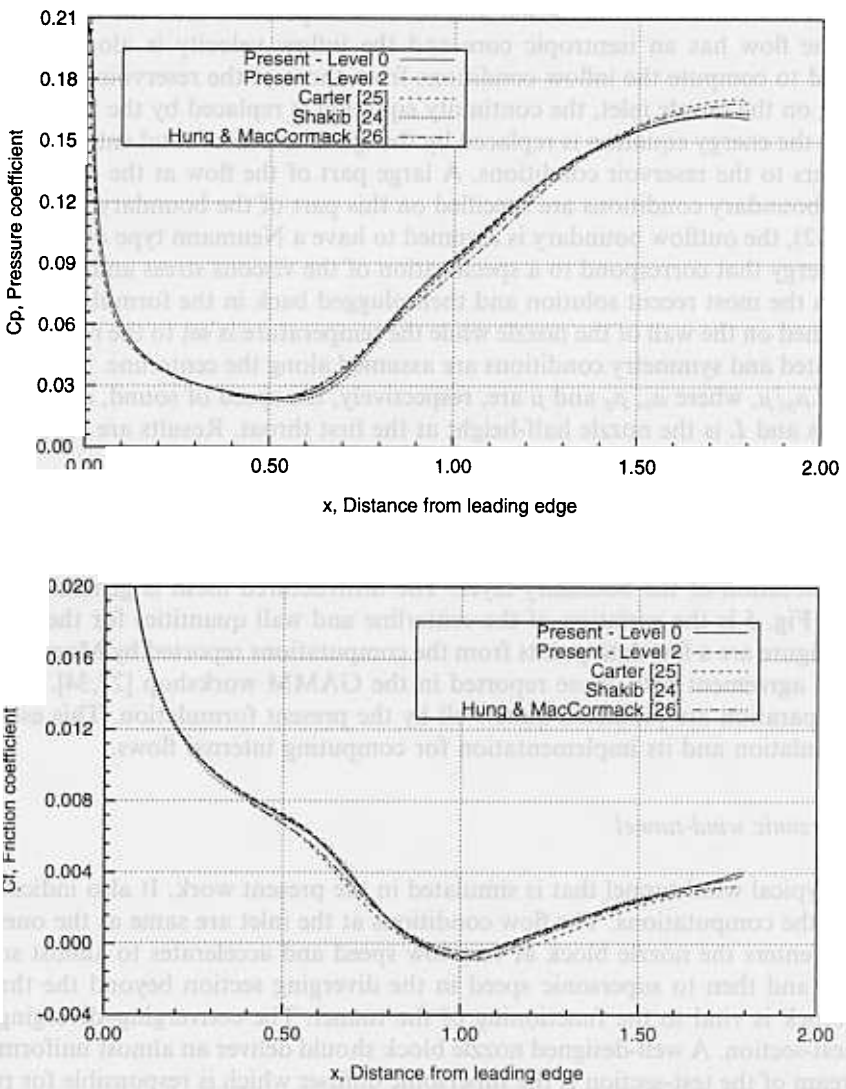

Fig. 2. $Re = 16{,}800$, $M = 3$ flow over a compression corner: the variation of the pressure and skin-friction coefficients along the solid surface for the steady-state solution.

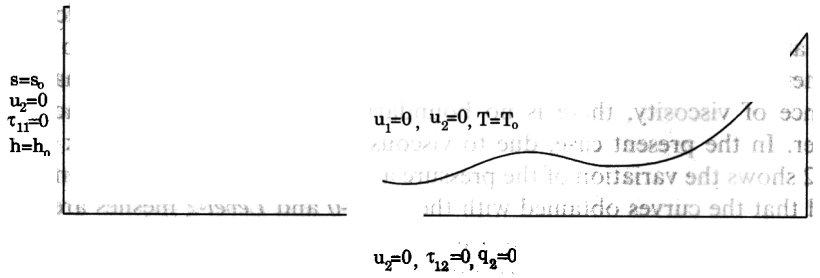

Fig. 3. Flow in a double throat nozzle: problem description.

other test problems in the workshop involve external flow past a *NACA 0012* airfoil. These flow problems have now become standard test cases for the purpose of validation of codes. The solutions with the present formulation for the external flow problem have been reported in paper by Mittal [18,19] and compare well with results from other researchers. Fig. 3 shows a schematic of the double throat nozzle problem along with the boundary conditions. The details of the geometry of the nozzle wall can be found in the paper by Bristeau et al. [27]. Flow comes in from the left and becomes supersonic after the first throat. At the inlet it is assumed that the flow has an isentropic core and the inflow velocity is along the x-direction. This condition is utilized to compute the inflow conditions from those at the reservoir. In our implementation, for the nodes lying on the nozzle inlet, the continuity equation is replaced by the isentropic condition, i.e., $(p/\rho^{\gamma} = p_0/\rho_0^{\gamma})$ and the energy equation is replaced by the specification of total enthalpy $(h_0 = C_p T_0)$, where the subscript 0 refers to the reservoir conditions. A large part of the flow at the exit section is supersonic and, therefore, no boundary conditions are specified on this part of the boundary. In our implementation, according to Eq. (22), the outflow boundary is assumed to have a Neumann type of boundary condition on the velocity and energy that correspond to a specification of the viscous stress and heat flux vectors. These are computed from the most recent solution and then plugged back in the formulation. No-slip condition for velocity is assumed on the wall of the nozzle while the temperature is set to the reservoir value. Only half the nozzle is simulated and symmetry conditions are assumed along the centerline. The Reynolds number is defined as $Re = a_0 L \rho_0/\mu$, where a_0, ρ_0 and μ are, respectively, the speed of sound, density and viscosity for reservoir conditions and L is the nozzle half-height at the first throat. Results are reported for $Re = 1600$. The computations are initiated from a uniform $M = 0.4$ flow.

Fig. 4 shows the *Level-2* mesh, and the flow field for the steady-state solutions. The finite-element mesh comprises of a structured part close to the wall and an unstructured component away from it. The structured part of the mesh allows one to have stretched elements close to the wall and therefore, more control over the resolution of the boundary-layer. The unstructured mesh is generated using Delaunay's method. Shown in Fig. 5 is the variation of the centerline and wall quantities for the computed solution. Also shown in the figure are a few data points from the computations reported by Marx [34]. Our computed solution is in good agreement with those reported in the GAMM workshop [27,34]. The location of the shocks and flow separation are predicted quite well by the present formulation. This establishes our confidence in the formulation and its implementation for computing internal flows.

4.3. Flow in a supersonic wind-tunnel

Fig. 6 shows a typical wind-tunnel that is simulated in the present work. It also indicates the boundary conditions used in the computations. The flow conditions at the inlet are same as the ones in the previous problem. The flow enters the nozzle block at very low speed and accelerates to almost sonic speed in the converging section and then to supersonic speed in the diverging section beyond the throat. A carefully designed nozzle block is vital to the functioning of the tunnel. The converging–diverging nozzle block is followed by the test-section. A well-designed nozzle block should deliver an almost uniform flow to the test-section. Downstream of the test-section is the supersonic diffuser which is responsible for pressure recovery at the expense of slowing down the flow. The diffuser is designed to produce an oblique shock train to minimize losses related with shocks. The flow in the diffuser is extremely complex and involves shock-wave/

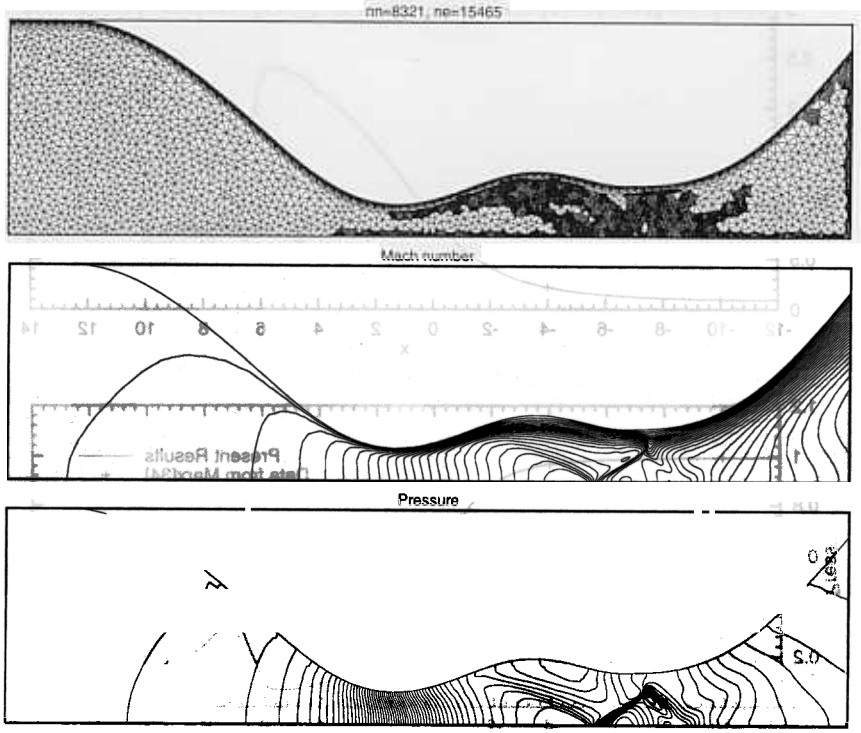

Fig. 4. $Re = 1600$ flow in a double throat tunnel: the *Level-2* mesh and the computed flow field for the steady-state solution.

boundary-layer interactions. A badly designed diffuser may either result in *unstarting* the tunnel or extremely poor efficiency. In Fig. 6, the test-section is of length L_t and half-height A_1. The various parameters that influence the performance of the wind-tunnel are the design of the nozzle block, A_2/A_1, L_t, L_c, L_s, the convergent and divergent angles in the diffuser section and the pressure ratio p_o/p_e. In the present work, the convergent and divergent angles of the diffuser are fixed to 10° and the effect of other parameters on the tunnel performance are studied. At the upstream boundary the stagnation pressure (p_o) and total enthalpy (h_o) are specified along with the direction of the flow (along the x-axis). The flow velocity at the inlet is unknown and so is the density. It is assumed that the flow between the reservoir and upstream boundary is isentropic and this condition is used to relate the density and pressure at the upstream boundary to the ones at reservoir (stagnation values). The walls of the tunnel are assumed to be maintained at the stagnation temperature and the velocity satisfies the no-slip condition. At the tunnel exit, a pressure value is specified and the viscous stress vector is assigned a zero value. To save on the computational expenses, only one half of the tunnel is simulated and symmetry conditions are imposed along the tunnel centerline: the vertical component of the velocity is set to zero and so are the viscous and heat flux vectors. All the boundary conditions are implemented in an *implicit* manner that leads to their strong enforcement and minimizes the associated numerical instabilities. The computations are initiated with zero flow condition and the pressure in the entire domain is initialized to a value corresponding to the exit pressure (p_e). The pressure at the inlet is ramped to its final value ($= p_o$) in 100 time units (non-dimensionalized with respect to the test-section half height, A_1 and the speed of sound at reservoir). Physically, this corresponds to the linear opening of the valve downstream of the pressurized gas tank for the blow-down. The time step used in the computation is 0.1. The Reynolds number, based on the half-height of the test-section (A_1), design speed of flow in the test-section, density and viscosity at reservoir conditions, is 5×10^5. The finite-element mesh consists of a few layers of structured mesh close to the tunnel walls and the rest of the domain is filled with an unstructured mesh obtained via Delaunay's triangulation.

It is well known that the second throat (in the diffuser section) plays an important role in the starting up of a supersonic tunnel. If the second throat is smaller than a certain value that is required for the start-up shock to pass through, the tunnel may *unstart*. Fig. 7 shows results for such a situation. In this simulation

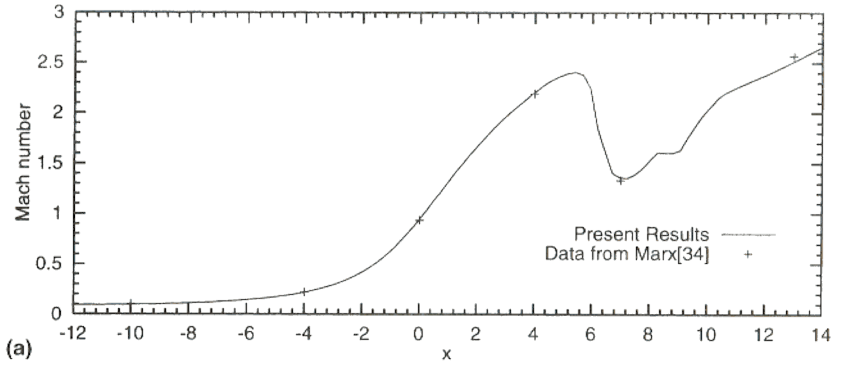

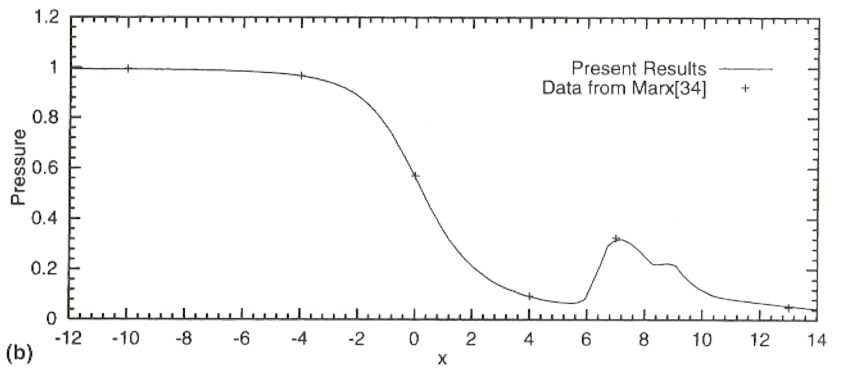

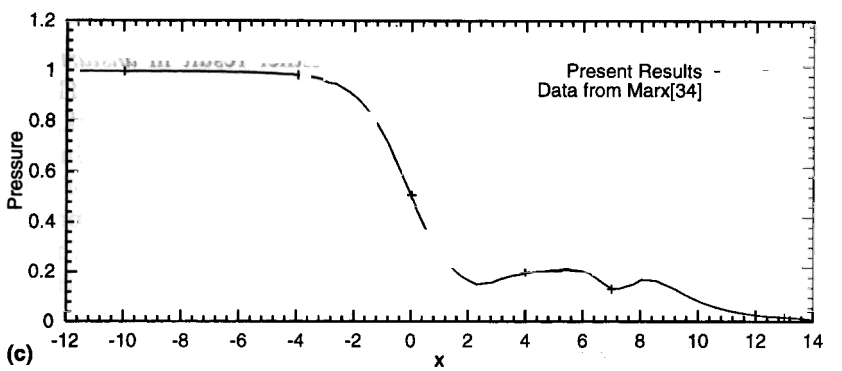

Fig. 5. $Re = 1600$ flow in a double throat tunnel: the flow field for the steady-state solution computed with the *Level-2* mesh; (a) centerline Mach number distribution; (b) centerline pressure distribution; (c) wall pressure distribution.

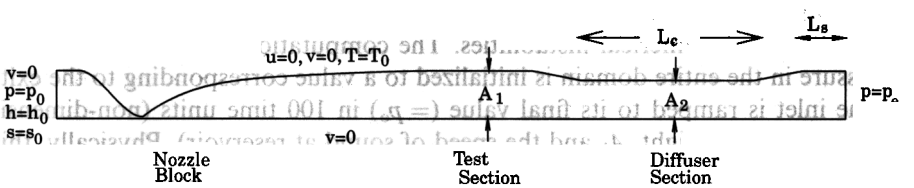

Fig. 6. Flow in a supersonic wind-tunnel: problem description.

the tunnel has a nozzle block whose test-section to throat area ratio (A_1/A_t) is 25. The nozzle block has been designed by using the method of characteristics for a minimum length nozzle to result in an inviscid Mach 5 flow. No correction for the boundary-layer thickness has been made in calculating the nozzle geometry. The test-section length (L_t) is 1.5, diffuser converging angle is 7.5°, length of constant-area section of diffuser

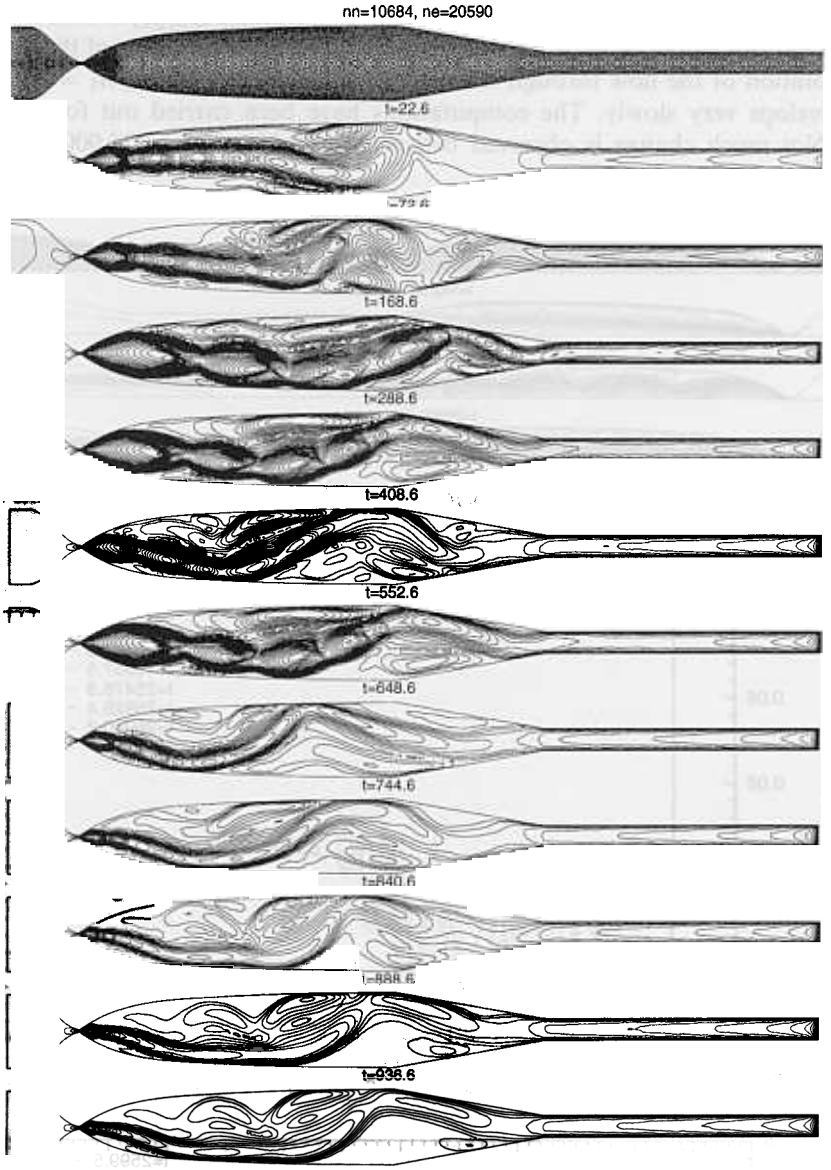

Fig. 7. Flow through a supersonic wind-tunnel, $A_2/A_1 = 0.3$, $p_o/p_e = 500$, $L_t = 1.5$, $L_c = 3.5$, $L_s = 0.0$: the finite-element mesh and the iso-mach contours for various time instants.

(L_c) is 3.5 and A_2/A_1 is 0.3. The ratio of the reservoir to exit pressure (p_o/p_e) is 500. From the inviscid flow theory, it is possible to estimate the minimum area of the diffuser required for allowing the start-up shock to pass through [2]. It is given as $A_2/A_t = p_{01}/p_{02}$, where p_{01}/p_{02} is the pressure ratio across a normal shock for the test-section Mach number. For a Mach 5 flow in the test-section and for $A_1/A_t = 25$, the minimum value of A_2/A_1 to start the tunnel is 0.6481. For viscous flows, the minimum area requirement is going to be even larger. It can be observed that, as expected, despite the very large pressure ratio, our computations indicate that the tunnel fails to start. In the early stages of the simulation, as the upstream pressure builds up, the flow develops in the nozzle and appears like an overexpanded jet. The pulsating behavior of the flow and the attraction of the jet towards the tunnel wall due to *Coanda effect* can be observed from the figure.

4.3.1. Nozzle block designed by using method of characteristics; $L_t = 2.0$; effect of A_2/A_1, p_o/p_e and L_c

The next set of computations are carried out for a tunnel with the same nozzle block as described above. The test-section length (L_t) is 2.0, diffuser converging–diverging angle is 10.0° and length of constant-area

section of diffuser (L_c) is 12.0. The ratio of the reservoir to exit pressure (p_o/p_e) is fixed at 25. Computations are carried out for various values of A_2/A_1 to study its effect on the performance of the tunnel. Figs. 8 and 9 show the time evolution of the flow through the tunnel for a diffuser with $A_2/A_1 = 0.6$. Beyond a certain time, the flow develops very slowly. The computations have been carried out for a very large non-dimensional time. Not much change is observed between $t = 10{,}000$ and $t = 25{,}000$. Therefore, it can be

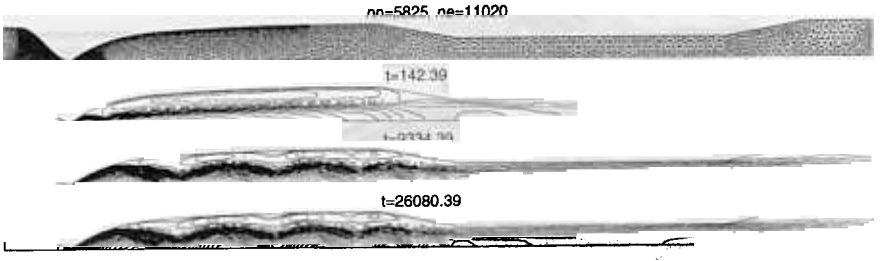

Fig. 8. Flow through a supersonic wind-tunnel, $A_2/A_1 = 0.6$, $p_o/p_e = 25$, $L_t = 2.0$, $L_c = 8.0$, L 2.0: the finite-element mesh and the iso-mach contours for various time instants.

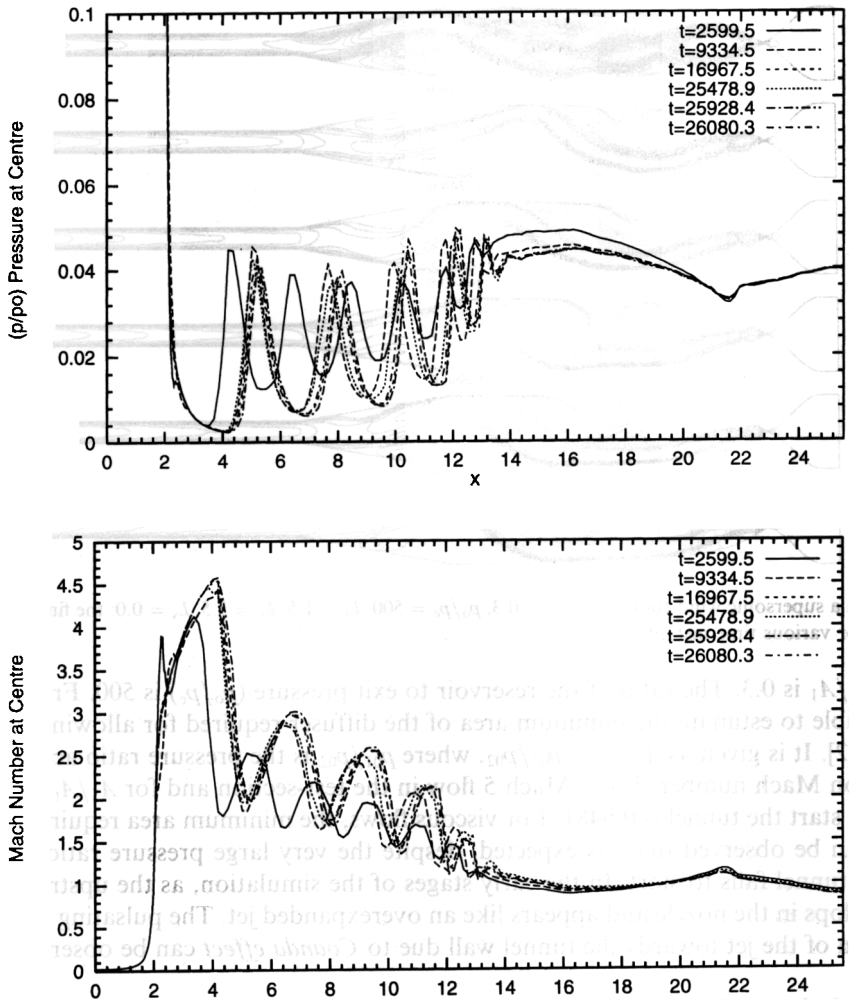

Fig. 9. Flow through a supersonic wind-tunnel, $A_2/A_1 = 0.6$, p_o/p_e 25, $L_t = 2.0$, $L_c = 8.0$, L 2.0: variation of pressure and Mach number along the tunnel centerline for various time instants.

concluded that the tunnel fails to start with this diffuser geometry too. This is consistent with the estimate of the minimum area requirement of the diffuser throat and increases our confidence in the present computations. Unlike the simulation for $A_2/A_1 = 0.3$, only half the tunnel has been simulated in the present case. This is not really appropriate if one is interested in the actual transient dynamics of the flow. For example, the flow that has been calculated in the previous case is far from being symmetric. However, in the present case, symmetry conditions have been imposed at the tunnel centerline which is certainly not the correct thing to do. In the present work, our interest lies in demonstrating our capability in using the stabilized finite-element method in the design of optimal supersonic tunnels. Therefore, to minimize on the computational requirement, rest of the computations in the paper are carried out with one half of the tunnel with the understanding that the present results give a qualitative picture of the effect of various parameters. If one is interested in the true transient dynamics, the computational domain must include the complete tunnel, at least for the cases that involve flow separation at the tunnel walls. Fig. 9 shows the centerline Mach number and pressure at various time instants of the simulation. The flow separates from

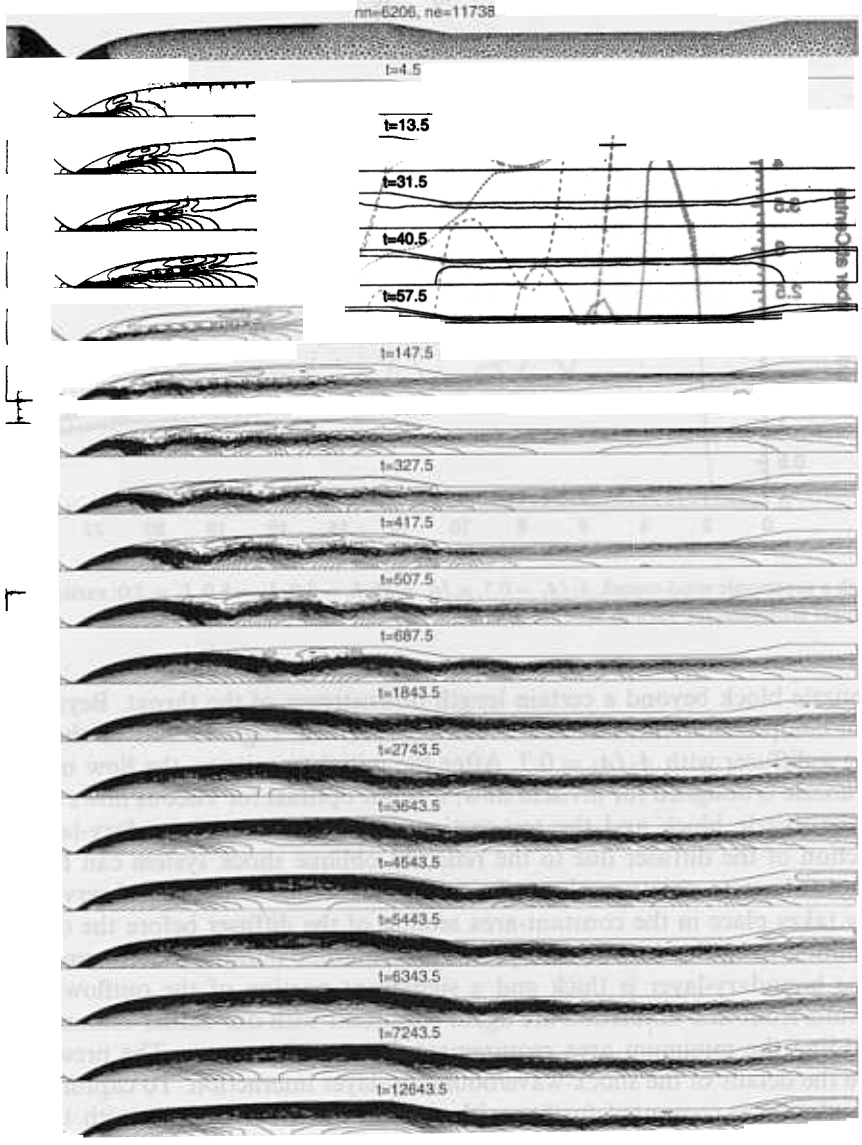

Fig. 10. Flow through a supersonic wind-tunnel, $A_2/A_1 = 0.7$, $p_o/p_e = 25$, $L_t = 2.0$, $L_c = 8.0$, $L_s = 2.0$: the finite-element mesh and the iso-mach contours for various time instants.

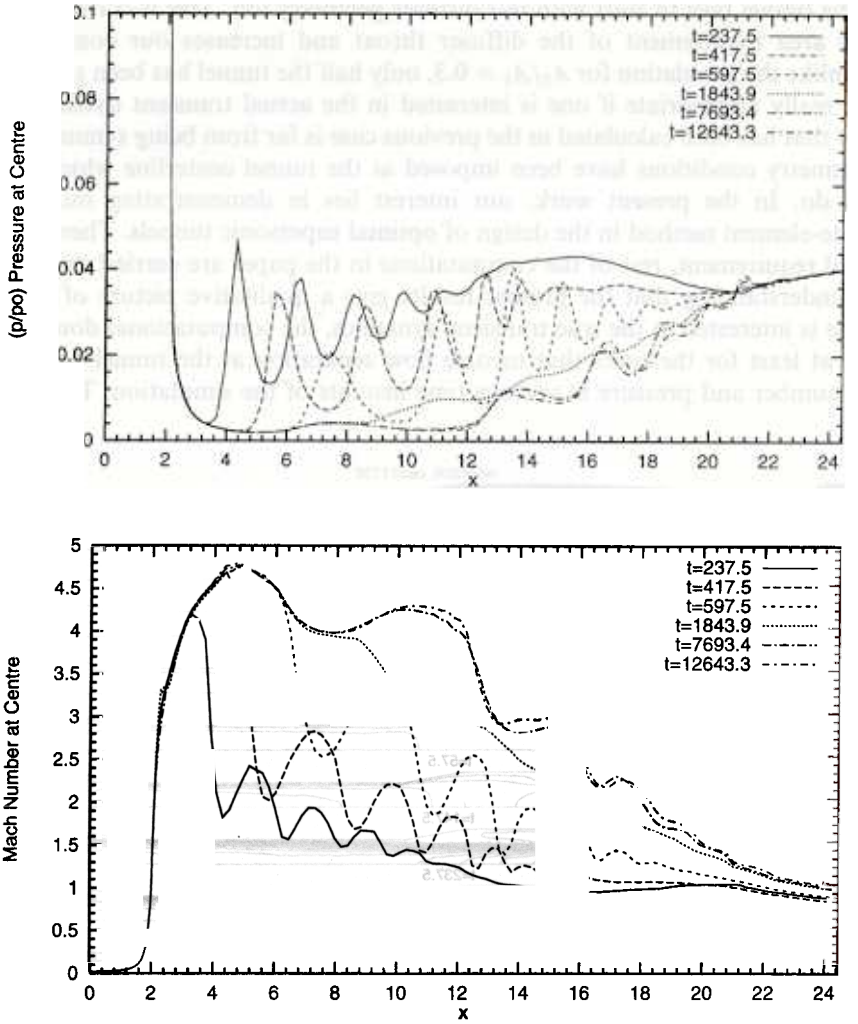

Fig. 11. Flow through a supersonic wind-tunnel, $A_2/A_1 = 0.7$, $p_o/p_e = 25$, $L_t = 2.0$, $L_c = 8.0$, $L_s = 2.0$: variation of pressure and Mach number along the tunnel centerline for various time instants.

the wall of the nozzle block beyond a certain length downstream of the throat. Beyond this distance, alternate regions of compression and rarefaction can be observed. Figs. 10 and 11 show the results of the computations for a diffuser with $A_2/A_1 = 0.7$. After the initial transience, the flow in the tunnel is established. Since the nozzle is designed for inviscid flow, it is not optimal for viscous flows and weak shocks can be observed in the nozzle block and the test-section. The undulating boundary-layer thickness in the constant-area section of the diffuser due to the reflected oblique shock system can be noticed. From the variation of the steady-state pressure along the tunnel centerline it can be observed that most of the pressure recovery takes place in the constant-area section of the diffuser before the divergent section and very little contribution from the downstream part. The centerline outflow Mach number is approximately 1.1. However, the boundary-layer is thick and a significant portion of the outflow close to the wall is subsonic. The results from this simulation are again consistent with our earlier estimates from the inviscid flow theory regarding the minimum area requirement for tunnel start-up. The present mesh is not fine enough to resolve the details of the shock-wave/boundary-layer interaction. To capture the details to some extent, the final solution is computed further with the *Level-2* mesh. Results with the *Level-2* mesh are shown in Fig. 12. The shocks in the nozzle block and their interaction with the boundary-layer can be observed more clearly in this solution. Also shown in the lower part of Fig. 12 is the variation of the centerline Mach number for the steady-state solution with the *Level-0* and *Level-2* meshes. As expected, the

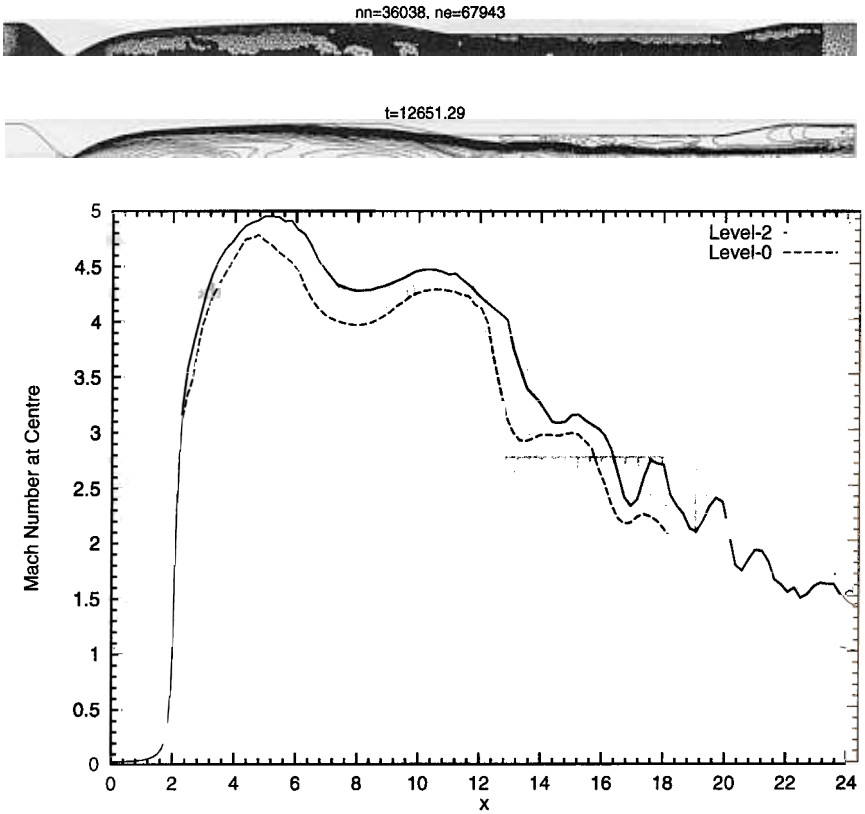

Fig. 12. Flow through a supersonic wind-tunnel, $A_2/A_1 = 0.7$, $p_o/p_e = 25$, $L_t = 2.0$, $L_c = 8.0$, $L_s = 2.0$: the finite-element mesh and iso-mach contours (top) for the *Level-2* solution. Shown below is the variation of the Mach number along the tunnel centreline for the steady-state solution.

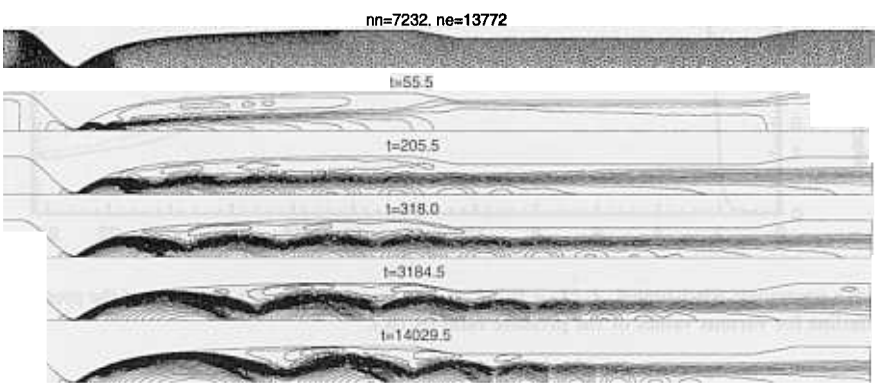

Fig. 13. Flow through a supersonic wind-tunnel, $A_2/A_1 = 0.8$, $p_o/p_e = 25$, $L_t = 2.0$, $L_c = 8.0$, $L_s = 2.0$: the finite-element mesh and the iso-mach contours for various time instants.

Level-2 solution picks up more details especially in the alternate regions of compression and rarefaction in the diffuser section. However, in a qualitative sense the two solutions result in very similar solutions. From the point of view of a designer who would like to have quick parametric solutions, the *Level-0* solution seems to be adequate. Results for $A_2/A_1 = 0.8$ are shown in Fig. 13. From these figures it can be concluded that the efficiency of the diffuser for this area ratio is lower than that for $A_2/A_1 = 0.7$. A shock in the nozzle block causes the flow to separate and consequently the core of the flow in the test-section is far from being one-dimensional. Perhaps, a higher pressure ratio p_o/p_e is needed to establish the flow in the tunnel with $A_2/A_1 = 0.8$. From this study it can be concluded that of all the cases studied so far, the diffuser with $A_2/A_1 = 0.7$ delivers the best results.

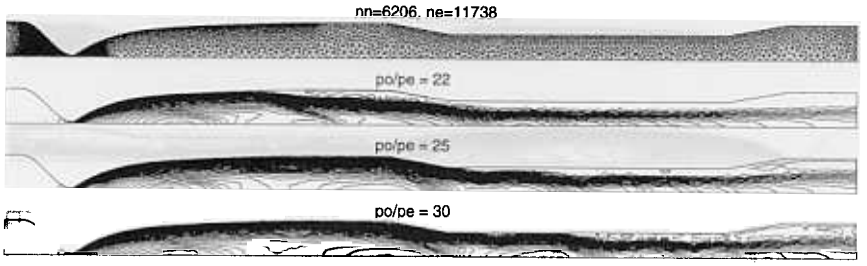

Fig. 14. Flow through a supersonic wind-tunnel, $A_2/A_1 = 0.7$, $L_t = 2.0$, $L_c = 8.0$, $L_s = 2.0$: the iso-mach contours for various values of the pressure ratio (p_o/p_e).

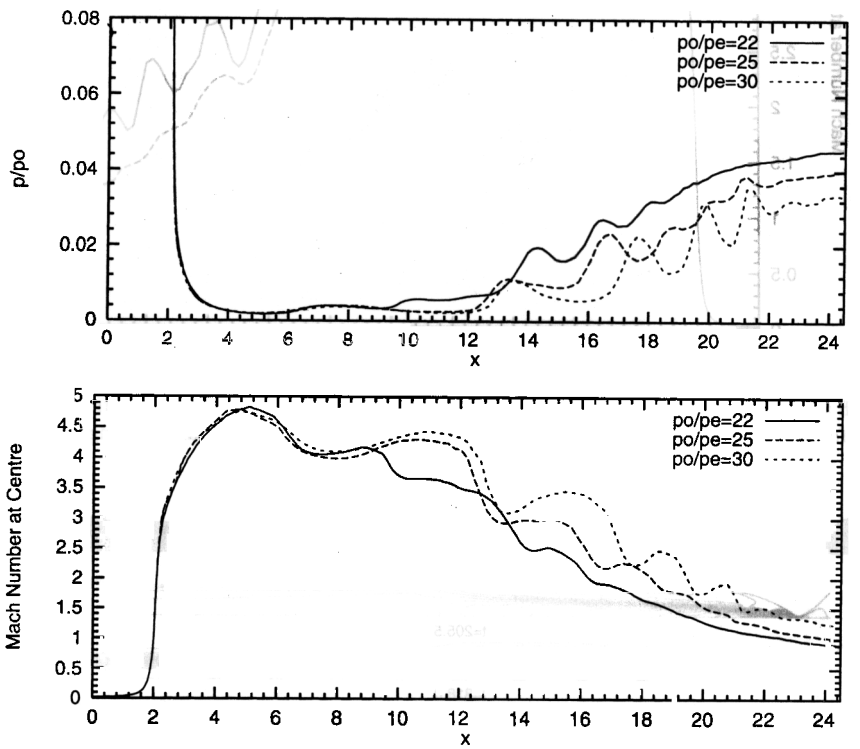

Fig. 15. Flow through a supersonic wind-tunnel, $A_2/A_1 = 0.7$, $L_t = 2.0$, $L_c = 8.0$, $L_s = 2.0$: variation of the pressure and Mach number along the tunnel centerline for various values of the pressure ratio (p_o/p_e).

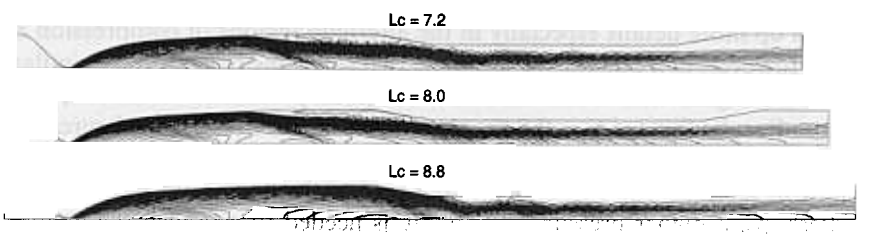

Fig. 16. Flow through a supersonic wind-tunnel, $A_2/A_1 = 0.7$, $p_o/p_e = 22$, $L_t = 2.0$, $L_s = 2.0$: the iso-mach contours for various values of the constant-area section length of the diffuser (L_c).

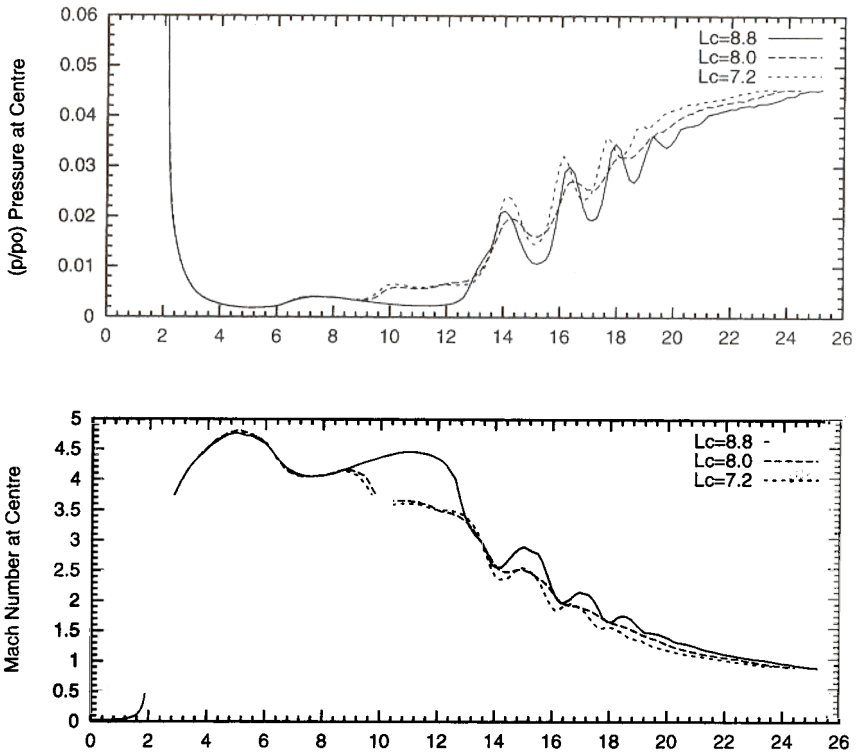

Fig. 17. Flow through a supersonic wind-tunnel, $A_2/A_1 = 0.7$, $p_o/p_e = 22$, $L_t = 2.0$, $L_s = 2.0$: variation of the pressure and Mach number along the tunnel centerline for various values of the constant-area section length of the diffuser (L_c).

In the next part of the study the effect of the reservoir to exit pressure ratio is investigated for the diffuser with $A_2/A_1 = 0.7$. Fig. 14 shows the steady-state solution for $p_o/p_e = 22$, 25 and 30. The corresponding variation of centerline pressure and Mach number is shown in Fig. 15. It can be observed that for $p_o/p_e = 25$ and 30 the flow in the test-section is almost same but significant differences are observed in the diffuser section. The separation point of the flow in the diffuser moves upstream as the pressure ratio decreases and at $p_o/p_e = 22$ reaches the later part of the nozzle block. From this study it is clear that the tunnel may not be able to start for p_o/p_e below 25 with the present diffuser section.

Having studied the effect of A_2/A_1 and p_o/p_e, the effect of the length of the constant-area section (L_c) of the diffuser is investigated. Computations are carried out for $A_2/A_1 = 0.7$, $p_o/p_e = 22$ and for $L_c = 8.8$, 8.0 and 7.2. Figs. 16 and 17 show the steady-state solutions for these three cases. In the cases with $L_c = 8.0$ and 7.2 the tunnel fails to provide a fully developed flow in the test-section. However, the case with $L_c = 8.8$ seems to result in an acceptable flow. It should be pointed out that the increase in the diffuser length may not always lead to an improvement in the flow quality. Beyond a certain length the losses due to friction (Fanno effect) may dominate and lead to a loss in the diffuser efficiency. This will also be highlighted in a calculation later in the paper.

4.3.2. Nozzle block with boundary-layer correction; effect of L_t, L_c and p_o/p_e

The nozzle block used in the computations in the previous section does not account for boundary-layer effects and results in a non-uniform flow in the tunnel test-section. This is not desirable and to rectify the situation a nozzle block with boundary-layer correction and $A_1/A_t = 30$ is utilized. The other parameters are $A_2/A_1 = 0.7$, $L_t = 2.0$, $L_c = 10.5$ and $L_s = 2.0$. Unlike the previous case, the tunnel does not deliver a satisfactory flow for $p_o/p_e = 25$. The computations for $p_o/p_e = 30$ are shown in Figs. 18 and 19. Compared to the earlier cases, the Mach number in the test-section is quite uniform as desired. Additionally, the time taken to reach the steady-state solution is much smaller compared to the previous cases. Figs. 20 and 21 show the effect of the test-section length (L_t) on the tunnel performance. In both

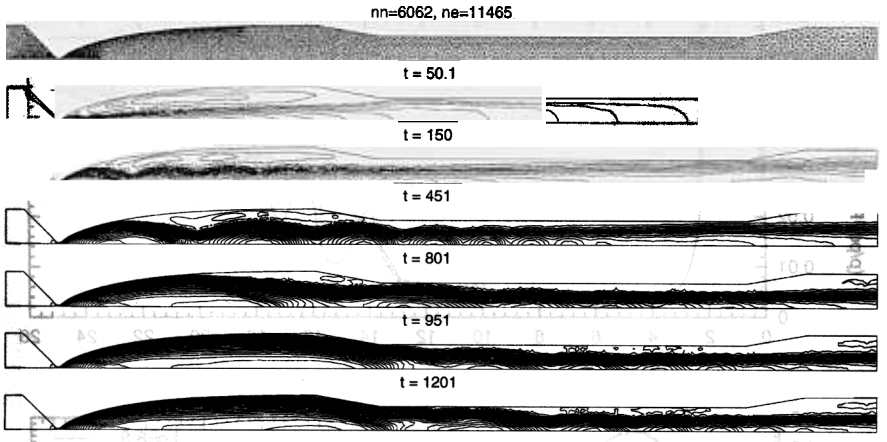

Fig. 18. Flow through a supersonic wind-tunnel, $A_2/A_1 = 0.7$, $p_o/p_e = 30$, $L_t = 2.0$, $L_c = 10.5$, $L_s = 2.0$: the finite-element mesh and the iso-mach contours for various time instants. The nozzle block has been designed using boundary-layer correction.

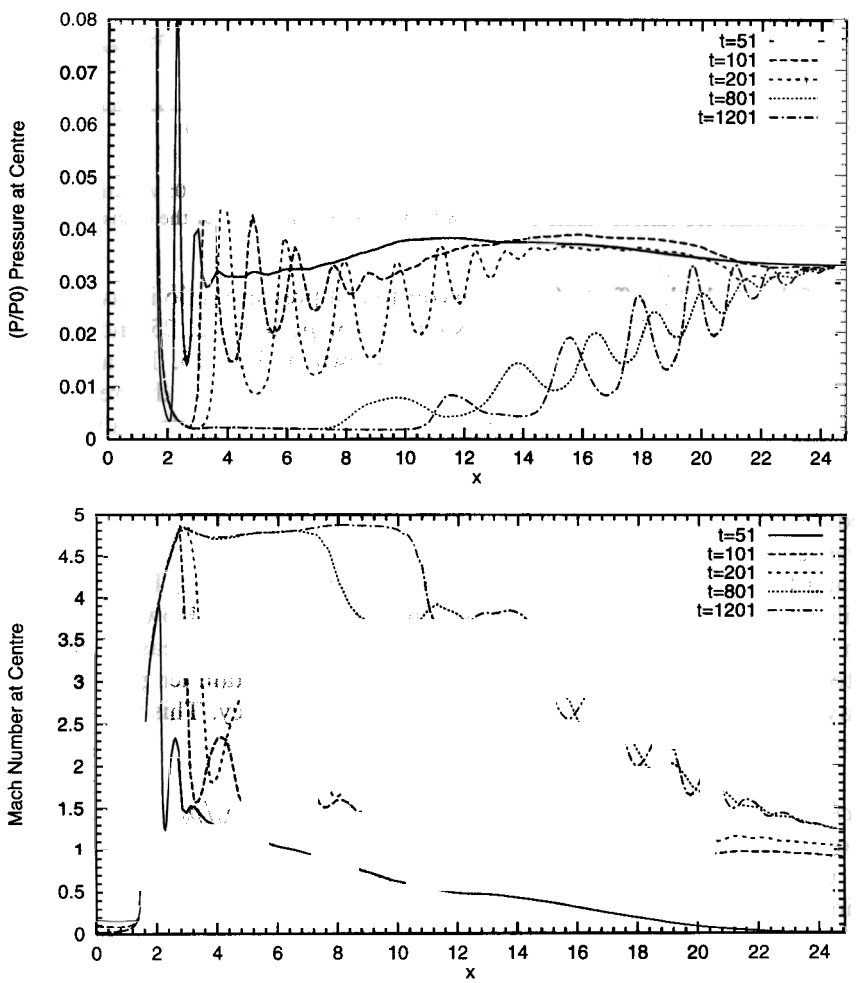

Fig. 19. Flow through a supersonic wind-tunnel, $A_2/A_1 = 0.7$, $p_o/p_e = 30$, $L_t = 2.0$, $L_c = 10.5$, $L_s = 2.0$: variation of pressure and Mach number along the tunnel centerline for various time instants. The nozzle block has been designed using boundary-layer correction.

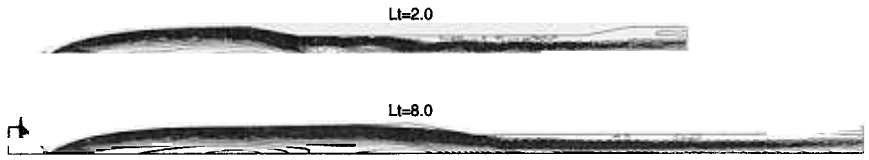

Fig. 20. Flow through a supersonic wind-tunnel, $A_2/A_1 = 0.7$, $p_o/p_e = 30$, $L_c = 10.5$, $L_s = 2.0$: the iso-mach contours for different values of the test-section length (L_t). The nozzle block has been designed using boundary-layer correction.

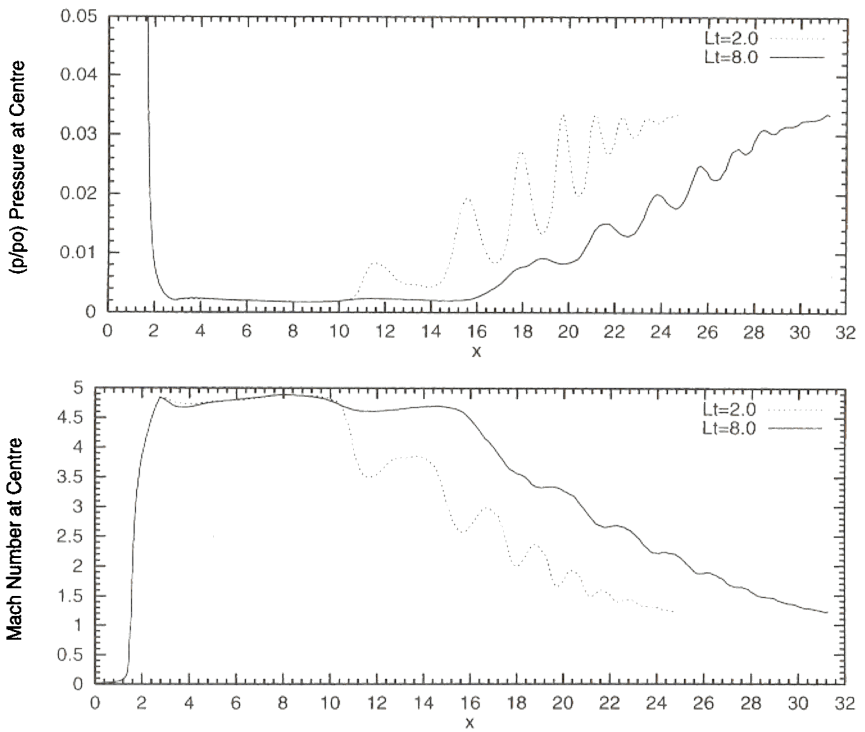

Fig. 21. Flow through a supersonic wind-tunnel, $A_2/A_1 = 0.7$, $p_o/p_e = 30$, $L_c = 10.5$, $L_s = 2.0$: variation of the pressure and Mach number along the tunnel centerline for different values of the test-section length (L_t). The nozzle block has been designed using boundary-layer correction.

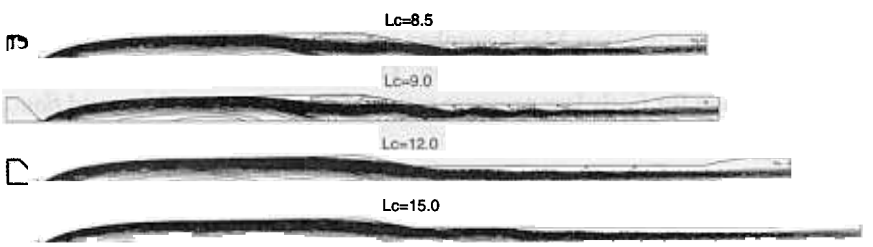

Fig. 22. Flow through a supersonic wind-tunnel, $A_2/A_1 = 0.7$, $p_o/p_e = 27$, $L_t = 8.0$, $L_s = 2.0$: the iso-mach contours for various values of the constant-area section length of the diffuser (L_c). The nozzle block has been designed using boundary-layer correction.

the cases the flow uniformity in the test-section is quite satisfactory. However, in the $L_t = 8.0$ case, the Mach number displays slight variation in the test-section. This suggests that the viscous losses in the test-section, that depend on L_t, play an important role in the optimal design of the diffuser. For the same reason, for $L_t = 8$, the effect of the length of the constant-area section of the diffuser (L_c) is studied for $p_o/p_e = 27$.

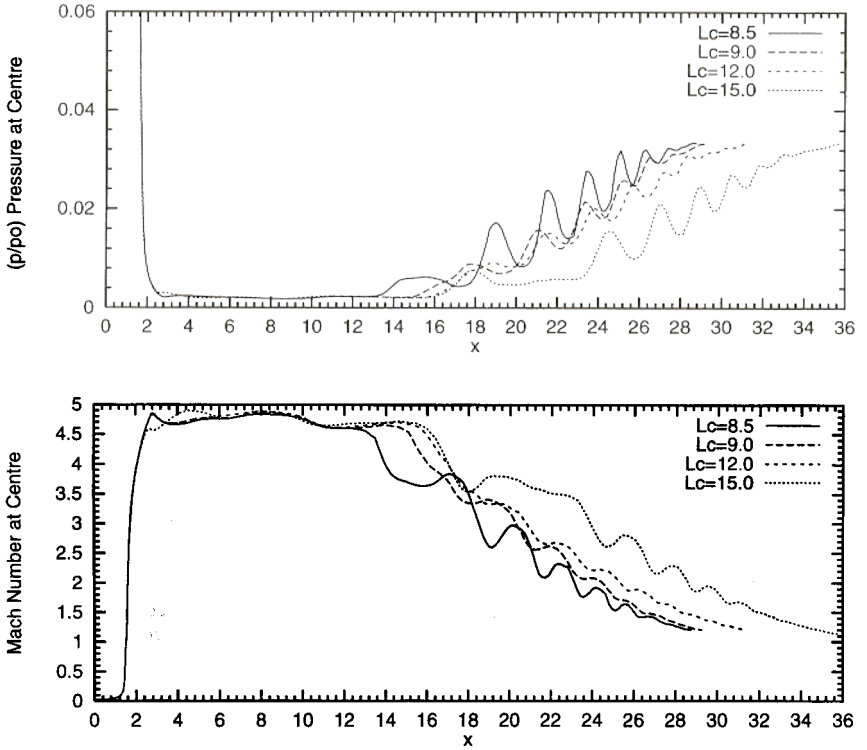

Fig. 23. Flow through a supersonic wind-tunnel, $A_2/A_1 = 0.7$, $p_o/p_e = 27$, $L_t = 8.0$, $L_s = 2.0$: variation of the pressure and Mach number along the tunnel centerline for the nozzle for various values of the constant-area section length of the diffuser (L_c). The nozzle block has been designed using boundary-layer correction.

Figs. 22 and 23 show the effect of L_c on the tunnel performance. It can be noticed that $L_c = 8.5$ and 9.0 result in flow separation in the test-section while $L_c = 12.0$ and 15.0 result in acceptable flow conditions in the the test-section. However, the mean Mach number in the test-section is significantly lower for $L_c = 15.0$ compared to that for $L_c = 12.0$. This suggests that the optimal value of L_c is close to 12.0. Fig. 24 shows the ratio of the stagnation pressure at the tunnel exit and entry for the steady-state solution for various values of L_c. This has been calculated by integrating the stagnation pressure across the tunnel cross-section at the two locations and indicates the extent of losses in the entire tunnel. As expected, the maximum value is achieved for $L_c = 12.0$ that signifies the minimal loss for that case amongst the for cases that have been studied. It is interesting to study the effect of pressure ratio p_o/p_e for $L_c = 15$. Figs. 25 and 26 show the steady-state solutions of the flow in the tunnel for $p_o/p_e = 25$, 27 and 30. In all the cases the flow develops in the test-section to an acceptable level but the test-section Mach number seems to depend on p_o/p_e. Smaller pressure ratios result in slightly lower Mach number in the test-section. This suggests that even though one may be able to establish flow in the test-section for fairly low pressure ratios, if one is interested in good *flow quality*, a higher pressure ratio must be employed.

5. Concluding remarks

Results have been presented for finite-element computations of viscous flows in supersonic wind-tunnels. The formulation has been tested on two benchmark problems involving flow in a double throat nozzle and Mach 3 flow past a 10° compression corner. The results are in good agreement with those from other researchers. The computations for the wind-tunnel are capable of simulating the start-up dynamics. If the diffuser throat is not large enough to allow the start-up normal shock to pass through the tunnel it *unstarts*. Our computations result in the same observation. The efficiency of the tunnel is intimately related to the

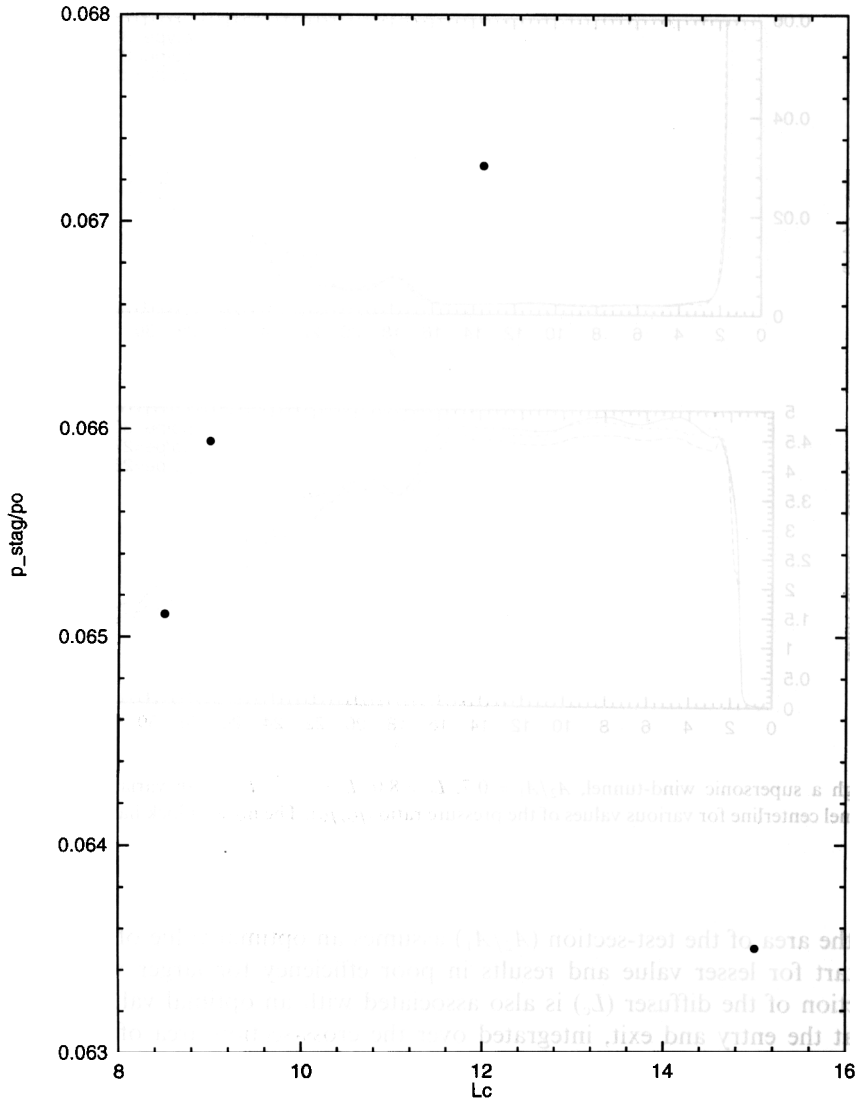

Fig. 24. Flow through a supersonic wind-tunnel, $A_2/A_1 = 0.7$, $p_o/p_e = 27$, $L_t = 8.0$, $L_s = 2.0$: ratio of the exit to entry stagnation pressure (integrated over the tunnel cross-section) for the various values of L_c. The nozzle block has been designed using boundary-layer correction.

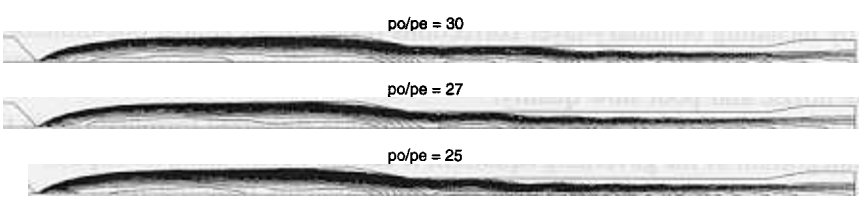

Fig. 25. Flow through a supersonic wind-tunnel, $A_2/A_1 = 0.7$, $L_t = 8.0$, $L_c = 15.0$, $L_s = 2.0$: the iso-mach contours for various values of the pressure ratio (p_0/p_e). The nozzle block has been designed using boundary-layer correction.

diffuser efficiency. One would like to establish a uniform flow in the test-section with the minimum value of the ratio of the reservoir stagnation to exit pressure ratio. The efficiency of the diffuser depends on a variety of parameters and their effect has been investigated in this paper. The ratio of the constant-area section of

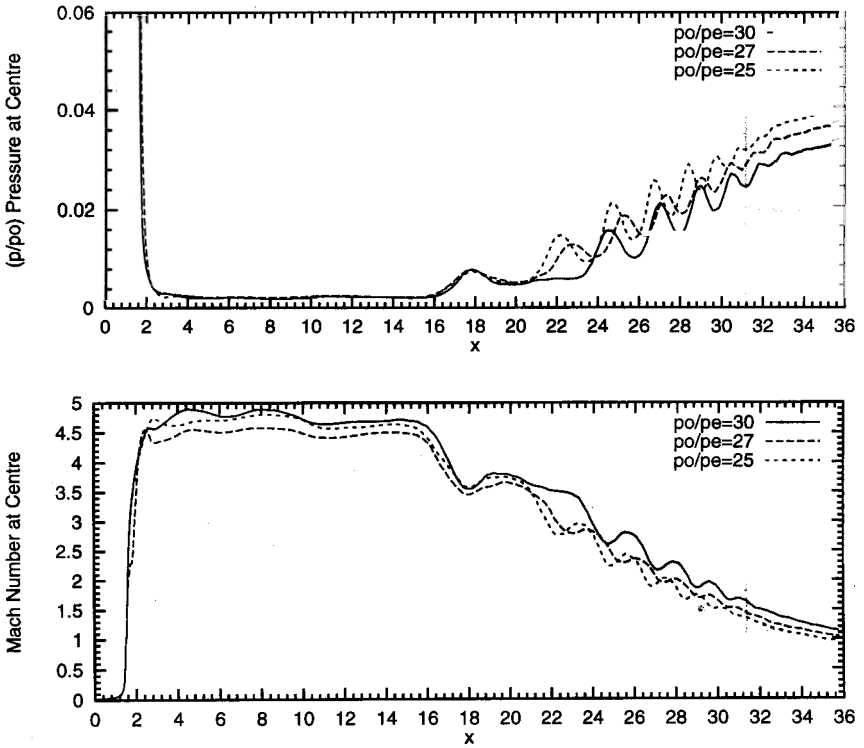

Fig. 26. Flow through a supersonic wind-tunnel, $A_2/A_1 = 0.7$, $L_t = 8.0$, $L_c = 15.0$, $L_s = 2.0$: variation of the pressure and Mach number along the tunnel centerline for various values of the pressure ratio (p_0/p_e). The nozzle block has been designed using boundary-layer correction.

the diffuser and the area of the test-section (A_2/A_1) assumes an optimal value of, approximately, 0.7. The tunnel fails to start for lesser value and results in poor efficiency for larger values. The length of the constant-area section of the diffuser (L_c) is also associated with an optimal value. The ratio of the stagnation pressure at the entry and exit, integrated over the cross-section area of the tunnel, indicates the extent of losses in the tunnel due to shocks and viscous effects. It has been shown in this paper that the losses are minimal for a certain value of L_c. The test-section length L_t affects the viscous losses in the tunnel and is responsible for certain amount of diffusion of flow even before it reaches the diffuser. A diffuser section that is optimal for a given value of L_t may not be so for a different test-section length. It has also been shown, that in certain cases, though it may be possible to start the tunnel with a low stagnation-to-exit pressure ratio, a higher pressure ratio may be desirable for a better flow quality in the test-section. The nozzle block also plays an extremely important role in the quality of flow in the test-section. A nozzle block that is designed by including boundary-layer corrections results in an almost one-dimensional flow in the test-section. On the other hand, a nozzle block that is deigned by the inviscid flow theory only leads to weak shocks within the nozzle and poor flow quality.

The finite-element methods used for the computations utilize stabilized formulations in the conservation variables. Time-integration of the governing equations is carried out by using an implicit implementation of the generalized trapezoidal rule. The large-scale equation systems resulting from the finite-element discretization of the flow problem are solved using a matrix-free implementation of the GMRES technique in conjunction with block-diagonal preconditioners. In some of the problems, the enhanced-discretization interface-capturing technique (EDICT) has been utilized to improve the accuracy of the base method. Typically, this technique leads to enhanced discretization of those regions in the computational domain that involve boundary/shear-layers, shock-waves and their interactions. It has been demonstrated that the numerical method can be used as an effective tool in the design and analysis of hardware for high-speed flows.

References

[1] J.D. Anderson, Gasdynamic Lasers: An Introduction, Academic Press, New York, 1976.
[2] J.D. Anderson, Modern Compressible Flow: with Historical Perspective, second ed., McGraw-Hill, New York, 1990.
[3] A. Hamed, J.S. Shang, Survey of validation data base for shockwave boundary-layer interactions in supersonic inlets, J. Propulsion Power 7 (4) (1991) 617–625.
[4] S.T. Polsky, J.L. Cambier, Numerical study of transient flow phenomena in shock tunnels, AIAA J. 32 (5) (1994) 971–978.
[5] C.L. Chen, S.R. Chakravarthy, Numerical investigation of separated nozzle flows, AIAA J. 32 (9) (1994) 1836–1843.
[6] B.M. Argrow, G. Emanuel, Computational analysis of the transonic flow field of two-dimensional minimum length nozzles, J. Fluids Eng., Trans. ASME 113 (1991) 479–488.
[7] D.M. Causon, D.M. Ingram, G. Yang, On applications of high resolution shock capturing methods to unsteady flows, in: E.F. Toro, J.F. Clarke (Eds.), Numerical Methods for Wave Propagation, Fluid Mechanics and its Applications, vol. 47, Kluwer Academic Publishers, Dordrecht, 1995, pp. 145–171.
[8] D.R. Reddy, L.J. Weir, Three-dimensional viscous analysis of a Mach 5 inlet and comparison with experimental data, J. Propulsion Power 8 (2) (1992) 432–440.
[9] W.J. Chyu, G.W. Howe, T.I-P. Shih, Bleed boundary conditions for numerically simulated mixed-compression supersonic inlet flow, J. Propulsion Power 8 (4) (1992) 862–868.
[10] A. Fujimoto, N. Niwa, K. Sawada, Numerical investigation of supersonic inlet with realistic bleed and bypass systems, J. Propulsion Power 8 (4) (1992) 857–861.
[11] Y.C. Hsia, B.J. Gross, J.P. Ortwerth, Inviscid analysis of a dual mode scramjet inlet, J. Propulsion Power 7 (6) (1991) 1030–1035.
[12] Y.C. Hsia, E.W. Daso, V.A. Padhye, Full Navier–Stokes analysis of a three-dimensional scramjet inlet, J. Propulsion Power 8 (5) (1992) 1071–1078.
[13] Y.C. Hsia, Full Navier–Stokes analysis of an axisymmetric scramjet inlet, J. Propulsion Power 9 (6) (1993) 827–833.
[14] J.J. Korte, D.J. Singh, A. Kumar, A.A. Auslender, Numerical study of the performance of swept, curved, compression surface scramjet inlets, J. Propulsion Power 10 (6) (1994) 841–847.
[15] T.E. Tezduyar, T.J.R. Hughes, Development of time-accurate finite element techniques for first-order hyperbolic systems with particular emphasis on the compressible Euler equations, Report prepared under NASA-Ames University Consortium Interchange, No. NCA2-OR745-104, 1982.
[16] T.E. Tezduyar, T.J.R. Hughes, Finite element formulations for convection dominated flows with particular emphasis on the compressible Euler equations, in: Proc. AIAA 21st Aerospace Sciences Meeting, Reno, NV, AIAA Paper 83-0125, 1983.
[17] T.J.R Hughes, T.E. Tezduyar, Finite element methods for first-order hyperbolic systems with particular emphasis on the compressible Euler equations, Comput. Methods Appl. Mech. Eng. 45 (1984) 217–284.
[18] S. Mittal, Finite element computation of unsteady viscous compressible flows, Comput. Methods Appl. Mech. Eng. 157 (1998) 151–175.
[19] S. Mittal, Finite element computation of unsteady viscous compressible flows past stationary airfoils, Comput. Mech. 21 (1998) 172–188.
[20] T.E. Tezduyar, S. Aliabadi, M. Behr, Enhanced-discretization interface-capturing technique, in: Proc. ISAC'97 High Performance Computing on Multiphase Flows, Tokyo, Japan, 1997.
[21] T.E. Tezduyar, S. Aliabadi, M. Behr, Enhanced-discretization interface-capturing technique (EDICT) for computation of unsteady flows with interfaces, Comput. Methods Appl. Mech. Eng. 155 (1998) 235–248.
[22] S. Mittal, S. Aliabadi, T. Tezduyar, Parallel computation of unsteady compressible flows with the EDICT, Comput. Mech. 23 (1999) 151–157.
[23] R. Lohner, An adaptive finite element scheme for transient problems in CFD, Comput. Methods Appl. Mech. Eng. 61 (1987) 323–338.
[24] F. Shakib, Finite element analysis of the compressible Euler and Navier–Stokes equations, PhD thesis, Department of Mechanical Engineering, Stanford University, 1988.
[25] J.E. Carter, Numerical solutions of the Navier–Stokes equations for the supersonic laminar flow over a two-dimensional compression corner, NASA Technical Report NASA TR R-385, NASA, 1972.
[26] C.M. Hung, R.W. MacCormack, Numerical solutions of supersonic and hypersonic laminar compression corner flows, AIAA J. 14 (4) (1976) 475–481.
[27] M.O. Bristeau, R. Glowinski, J. Periaux, H. Viviand, Presentation of problems and discussion of results, in: M.O. Bristeau, R. Glowinski, J. Periaux, H. Viviand (Eds.), Numerical Simulation of Compressible Navier–Stokes Flows, Notes on Numerical Fluid Mechanics, vol. 18, Vieweg, Wiesbaden, 1987, pp. 1–40.
[28] Z. Johan, T.J.R. Hughes, F. Shakib, A globally convergent matrix-free algorithm for implicit time-marching schemes arising in finite element analysis in fluids, Comput. Methods Appl. Mech. Eng. 87 (1991) 281–304.
[29] S. Mittal, V. Kumar, A. Raghuvanshi, Unsteady incompressible flow past two cylinders in tandem and staggered arrangements, Int. J. Numer. Methods Fluids 25 (1997) 1315–1344.
[30] S.K. Aliabadi, T.E. Tezduyar, Space-time finite element computation of compressible flows involving moving boundaries and interfaces, Comput. Methods Appl. Mech. Eng. 107 (1993) 209–224.
[31] T.J.R. Hughes, M. Mallet, A new finite element formulation for computational fluid dynamics. IV. A discontinuity-capturing operator for multidimensional advective–diffusive systems, Comput. Methods Appl. Mech. Eng. 58 (1986) 329–339.
[32] Y. Saad, M. Schultz, GMRES: a generalized minimal residual algorithm for solving nonsymmetric linear systems, SIAM J. Sci. Statist. Comput. 7 (1986) 856–869.

[33] M. Sarkis, X.C. Cia, C. Farhat, Variable degree Schwarz methods for implicit solution of unsteady compressible Navier–Stokes equations on unstructured meshes, Technical Report 96-48, Institute for Computer Applications in Science and Engineering, NASA Langley Research Center, July 1996.

[34] Y. Marx, Computations for viscous compressible flows in a double throat nozzle, in: M.O. Bristeau, R. Glowinski, J. Periaux, H. Viviand (Eds.), Numerical Simulation of Compressible Navier–Stokes Flows, Notes on Numerical Fluid Mechanics, vol. 18, Vieweg, Wiesbaden, 1987.